Materials Advances

ROYAL SOCIETY OF CHEMISTRY

PAPER

View Article Online
View Journal | View Issue

Cite this: *Mater. Adv.*, 2024, 5, 1284

Synergistic enhancement of seawater hydrogen generation *via* sulfur vacancy enriched and phases engineered CQD loaded CdS photocatalyst†

Bishal Kumar Nahak[a] and Fan Gang Tseng *[abcde]

The use of photocatalytic water splitting, which involves generation of hydrogen (H_2), is regarded as a possible remedy to counteract the obstacles in the use of fossil fuels and to confront the issues of the energy crisis and environmental contamination. Despite the advancements, there continues to be a scarcity of research on stable and efficient photocatalysts suitable for use in seawater. The present paper describes the process of creating a photocatalyst using a hydrothermal method which combines carbon quantum dots and cadmium sulfide (CdS) nanoparticles. The developed photocatalyst showed excellent photocatalytic H_2 generation (80 450 μmol g^{-1} in 10 h) and dye degradation efficiency (97% in 60 min). Further, the H_2 generation of bare CdS and CQD@CdS was also tested under seawater conditions where a longer lifetime of particle was observed up to 10 h. A comprehensive analysis was conducted to evaluate the photodegradation mechanism of Rhodamine B dye utilizing the CQD@CdS system. The results showed that the process kinetics can be depicted using a pseudo-second order reaction. The remarkable catalytic activity and outstanding durability of the CQD@CdS can be ascribed to the effective function of the CQDs, which augment the segregation of the photoinduced charge carriers and averts the occurrence of photocorrosion in seawater. Moreover, the CQDs also supported a higher specific surface area and phase transformation in CdS with a dominant hexagonal phase. All these synergistic effects on the properties by the CQD@CdS, aided in creation of a highly efficient photocatalyst that is suitable for applying to solar hydrogen generation.

Received 20th September 2023,
Accepted 2nd December 2023

DOI: 10.1039/d3ma00741c

rsc.li/materials-advances

1. Introduction

Hydrogen (H_2) presently has an impressive position as one of the most viable and net zero carbon energy sources. Therefore, as the required global energy supply will continue to increase, the energy transition should be accompanied by efficient emerging technologies with worldwide availability.[1] Converting solar radiation into H_2 using a potent photocatalyst is regarded as a glimpse into the future for providing a sustainable resource to address energy concerns.[2–6] Driven by natural photosynthesis process, production of H_2 *via* solar water splitting has gained the interest of researchers over the decades, dating all the way back to 1972, when TiO_2 was first used for the electrochemical splitting of water in the presence of light.[7–10] Given the potential for converting the renewable solar irradiation and plentiful natural seawater into chemical fuels, immense efforts have been made in devising new efficient photocatalysts, particularly those capable of utilizing visible light (420–700 nm)[11–15] which accounts for approximately 43% of the solar spectrum.[16]

Photocatalytic techniques are very effective, low-cost, and environmentally beneficial for remediation of various organic contaminants. Numerous semiconductors with and without alterations have been extensively studied as potential photocatalysts for the mineralization of organic compounds such as CeO_2, Fe_2O_3, SnO_2, TiO_2, ZnO.[11,16–22] However, the larger band gap of these oxide semiconductors, means that the catalytic activity is limited to the UV region. Another key challenge for using oxide photocatalysts is that the quick charge carrier recombination has to be dealt with ref. 24 and 25.

Chalcogenide semiconductors were regarded as promising candidates for visible light responsive (VLR) hydrogen

[a] *Department of Engineering and System Science, National Tsing Hua University, Section 2, Kuang-Fu Rd, Hsinchu 30013, Taiwan, ROC. E-mail: fangang@ess.nthu.edu.tw; Fax: 886-3-5733054; Tel: 886-3-5715131 ext. 34270, 886-3-5733054*
[b] *Institute of Nano Engineering and Microsystems, National Tsing Hua University, Hsinchu 30013, Taiwan, ROC*
[c] *Department Chemistry, National Tsing Hua University, Hsinchu 30013, Taiwan, ROC*
[d] *Research Center for Applied Sciences, Academia Sinica, Taipei 11529, Taiwan, ROC*
[e] *Frontier Research Center on Fundamental and Applied Sciences of Matters, National Tsing Hua University, Hsinchu 300, Taiwan, ROC*

† Electronic supplementary information (ESI) available. See DOI: https://doi.org/10.1039/d3ma00741c

generation due to their intrinsic merits which include its favorable band gap, fast light response and excellent thermal stability.[25–27] Cadmium sulfide (CdS) is an ideal candidate for use as a VLR photocatalyst due to its narrow band gap of 2.4 eV. Because it has a small radius for the diffusion of photoinduced electrons and holes, it enables a bare CdS semiconductor to improve the solar light absorption and scattering capabilities, leading to a decrease of charge carrier recombination.[28] However, under continuous exposure to light, CdS has shown a low resistance towards photo-corrosion. Various capping agents have been utilized to increase the stability of these particles in the nanodomain.[29–31] This class of substances can act as a capping or passivating agent that decreases the energy required for the formation of new nuclei on a pre-existing structure by lowering the interfacial activation-energy.[32–36] Among these different passivating agents, poly(vinylpyrrolidone) (PVD) gained much interest because of its water solubility, biocompatibility and because it is relatively harmless to the environment.

Strategies for surface treatment have been utilized to minimize the recombination of charge carriers and to lessen the photocorrosion of CdS. The prevailing approach involves the implementation of sacrificial reagents (SRs) such as formic acid, lactic acid, S^{2-}, SO_3^{2-}, that effectively scavenge the photo-induced holes. Another way to enhance the photocatalytic performance, is by creating cationic/anionic vacancies[37] and using a co-catalyst such as TiO_2,[38,39] ZnO,[40,41] MoS_2,[42,43] ZnS,[44] Bi_2WO_6,[45] g-C_3N_4[46] and precious metals.[47] They may act as trap centers or electron acceptors for the photogenerated electron that help to reduce the recombination and boosts the CdS photocatalytic performance. However, these materials necessitate sophisticated, expensive processing equipment, use of harmful chemicals and at the same time they are not ecofriendly. Therefore, it is necessary to find an alternative cocatalyst that is ecofriendly, easy to synthesize and able to reduce charge carrier recombination.

Apart from these, some other alternatives have also been reported such as band-gap engineering and creating sulfur vacancies (SVs).[23] Band-gap engineering plays a crucial role in achieving an appropriate phase, and facilitating the effective separation of charge carriers. Yu *et al.*, reported cubic-phase CdS nanocrystals that were rich in sulfur, and which gave a hydrogen production rate of 680 μmol g^{-1} h^{-1}.[48] Similarly, Li *et al.*, produced hexagonal CdS nanorods with an H_2 generation efficiency of 740 μmol g^{-1} h^{-1}.[49] Some reports also claim that using multiple crystal phases or phase junctions in semiconductor crystals has been proven to enhance photocatalytic performance. Ai *et al.*, synthesized a mixed phase CdS nanostructure which had a suitable bonding width that improved the H_2 yield up to 4893 μmol g^{-1} h^{-1}.[50] Although the significance of these phase junctions was explored to some degree using the previously mentioned methods, they have not been given due consideration. Thus, additional investigations into the significance of phase junctions and the factors associated with them are still needed. Recently, anion vacancies have been one of the notable ways to create trap centers that capture the charge carriers. This has been quite common in narrow band gap semiconductors such as CdS, CdSe, SnS_2, and ZnS. Conventionally, SVs are created by doping, etching, and controlling the ratio of reactants in the synthesis process. However, individually, none of these factors were successful in increasing the H_2 generation efficiency to a great extent. Herein, a strategic increase of SVs was made with the addition of carbon quantum dots (CQDs) that helped in catalytic process. The presence of a synergistic effect between the mixed phase structure and SVs helped in lowering the photoinduced charge carrier recombination and provided a higher hydrogen evolution rate (HER).

The CQDs are a class of finely proportioned carbon-based nanomaterials that bear a resemblance to graphite particles. These carbonaceous materials are essential for facilitating the interaction between adsorbed O_2 on the surface and photoinduced electrons, thus preventing charge carrier's recombination.[51–53] The CQDs with a large specific Brunauer–Emmett–Teller (BET) area can be easily treated to anchor an array of functional groups, including –COOH, –OH, and –C═O.[54–56] Furthermore, the CQDs possess exceptional properties such as being excellent electron acceptors, having a unique electron reservoir, and they are also low-cost, non-toxic, and highly stable, making them a preferred cocatalyst in photocatalysis.[57–59] Using graphene as a highly effective cocatalyst in CdS photocatalytic systems has been extensively studied. However, nanosized CQDs offer several advantages such as easy functionalization and the ability to generate a large number of reducing sites that enhance charge separation and give a greater H_2 evolution.[57] Although CQDs have low electrical conductivity, they are a cost-effective alternative for forming heterojunctions with CdS. In addition, CQDs offer a high surface area and a highly porous morphology that can effectively adsorb various organic pollutants.[59] The functional groups present in CQDs can expertly interrupt the recombination process of the charge carriers in CdS.[58]

Recently, various techniques have been developed to create a near-coaxial heterojunction by uniformly attaching conjugated carbon layers to the surface of CdS during the nucleation stage of nanoparticles. Lei *et al.*, have published a study on the use of CdS nanoparticles combined with graphene quantum dots (GQDs) to boost the photocatalytic production of H_2. In their study, the GQDs acted as electron acceptors which reduced the charge recombination.[60] In a study by Guo *et al.*,[61] a solvothermal method was utilized to create a photocatalyst consisting of activated carbon fibers and CdS, derived from coal. The resulting material demonstrated an exceptional VLR photocatalytic performance in degrading methylene blue dye. In all these cases the enhancement of the H_2 evolution was claimed to be due to the presence of CQDs, where the CQDs acts as an electron acceptor that helps in reducing charge carrier recombination. However, as far as is known its influence on the change in phase transformation and creating sulfur-vacancies has not so far been reported. Herein, CQD-based CdS nanoparticles have been fabricated using a facial hydrothermal method. The main focus of this study is the design of a VLR

photocatalyst with a high surface area and mixed phase structure that increases H_2 evolution and stability of the pristine CdS. Furthermore, various characterizations have been performed to validate the properties of the sample. The developed photocatalyst was utilized for Rhodamine B (RhB) dye mineralization and H_2 generation in normal water and seawater.

2. Experimental

2.1. Materials

All the chemicals were of analytical grade and used without further purification. Cadmium acetate ($Cd(CH_3COO)_2$), thiourea ($(NH_2)_2CS$), sodium hydroxide (NaOH), glucose ($C_6H_{12}O_6$), urea ($CO(NH_2)_2$), methanol (MeOH) and triethylamine (TEA, $N(CH_2CH_3)_3$) were purchased from Sigma-Aldrich (USA). Deionized (DI) water (resistivity: 18.5 MΩ cm) was used for all the analyses. The detailed characterization details given in ESI† (Text S1).

2.2. Synthesis of the carbon quantum dots

A hydrothermal method was used to synthesize CQDs, with aqueous glucose as the reaction precursor. To begin with, 1 g of glucose and 50 mL of DI water was prepared at room temperature. The resulting solution was subjected to hydrothermal treatment at 200 °C for 12 h in a Teflon-lined stainless-steel autoclave. Upon cooling, the dark colored liquid was refined using a membrane with a pore diameter of 200 nm. It was then washed three times with ethanol to eliminate impurities, and centrifuged for 30 min at 10 000 rpm to separate the carbon containing liquid from a heavy black precipitate. The CQD solution was used for further experiments. The detailed procedure is shown in Scheme 1.

Nitrogen doped CQD (N-CQDs) was synthesized with urea as the nitrogen source. Urea (0.5 g) was mixed with the initial reagent and the process was carried out similar way.

2.3. Synthesis of the CQD@CdS photocatalyst

Typically, cadmium and sulfur salts were mixed in 1 : 1 mole ratio during the synthesis process. First, an aqueous solution of salts was prepared using $Cd(CH_3COO)_2$ as the source of Cd^{2+} ions and $(NH_2)_2CS$ for the S^{2-} ions. CdS nanoparticles have higher tendency to get agglomerated in nucleation stage, thus an aqueous poly(vinylpyrrolidone) (PVP) solution have been used as capping agent that helps CdS to remain in nanodomain. The PVP solution was mixed with the cadmium salt solution under stirring condition, until it became transparent. Next, the $(NH_2)_2CS$ solution was added dropwise to the previous solution under stirring and at a temperature of 75 °C. Finally, the pH of the solution was maintained at 11 using 2 N NaOH solution. As a result, a yellow colored solution was formed, which was transferred to a 100-mL Teflon-lined stainless-steel container and planed in autoclave at a temperature of 140 °C and left overnight. After the solution had cooled down to room temperature, the yellow colored precipitate was washed three times with DI water/ethanol to eliminate unwanted products. The particles were dried at 60 °C for 12 h, during which time the PVP@CdS formed (Scheme 1). Here, PVP@CdS has been used because bare CdS did not contain CQD.

The CQD@CdS samples were prepared by mixing the previously prepared CQDs from the initial CdS synthesis. In order to find optimal loading of CQD on CdS, different amounts (1 mL, 2 mL and 3 mL) of CQDs were used. Throughout the research 3 mL of CQD with CdS was used for different characterization and experimental purposes, due to its high performance (discussed in later sections). The rest of the procedure followed was similar to that used for PVP@CdS. Similarly, N-CQD@CdS was prepared using 3 mL of N-CQD at the reagent stage.

2.4. Photocatalytic experiment

2.4.1. Hydrogen generation. The hydrogen generation of the synthesized samples was performed using visible light assisted water splitting. In the experiment, 0.25 g of the

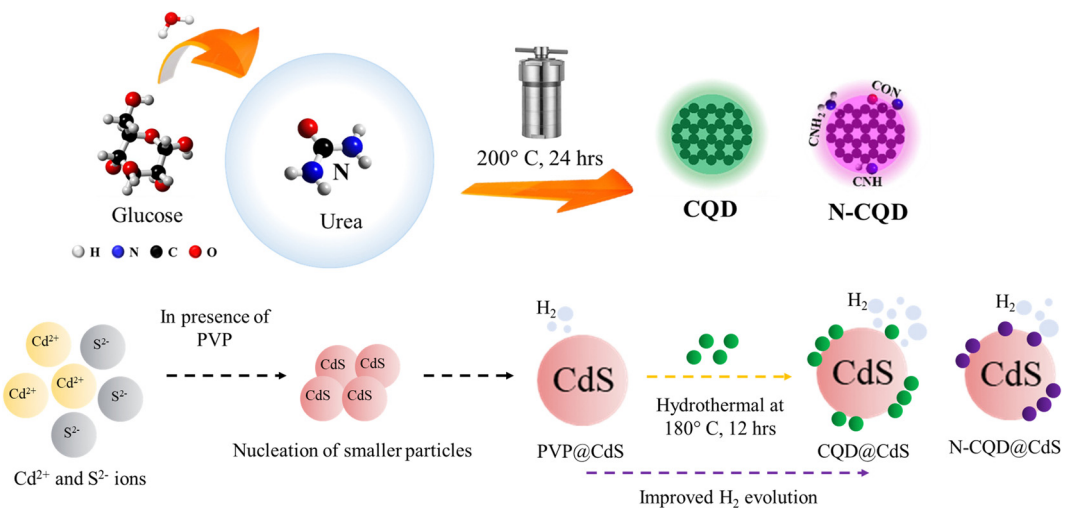

Scheme 1 This shows the synthesis process of carbon quantum dots (CQDs) and the CQD integrated cadmium sulfide photocatalyst.

CQD@CdS photocatalyst powder was mixed with 10.0 mL of DI water. To this mixture, MeOH and TEA were added in equal parts. The TEA acts as sacrificial electron donor and MeOH is used to reduce phase segregation between the TEA and water. The prepared solution was moved into a glass reactor and sealed with a serum plug. The solution was degassed by bubbling Ar through it for 20 min and mixing it ultrasonically. Next, under the stirring conditions the suspension was exposed to light from a 350-W Xe lamp, placed at a distance of 10 cm to attain a photon energy density of 1000 W m^{-2} and a cut-off filter was used to emit wavelengths greater than 400 nm. The evolved gas products were determined using a Shimadzu GC-2014 gas chromatograph (GC) with a gas-tight syringe in presence of Ar as carrier gas. The amount of H_2 generated was determined by referring to a standard hydrogen gas with known concentrations using a thermal conductivity detector. The apparent quantum yield (AQY) of the generated hydrogen gas was calculated using eqn (1):

$$\begin{aligned} \mathrm{AQY} &= \frac{\text{No. of reacted electrons}}{\text{No. of incident photons}} \times 100 \\ &= \frac{2 \times \text{No. of evolved hydrogen molecules}}{\text{No. of incident photons}} \times 100 \end{aligned} \quad (1)$$

2.4.2. Dye degradation. The RhB dye mineralization experiments involved using the 350-W Xe lamp. The model pollutant sample was prepared using 50 ppm of RhB, was mixed in 50 mL of DI water followed by the addition of 0.25 g of the photocatalyst. The solution was then exposed to light from a 350-W Xe lamp, placed at a distance of 10 cm to attain a photon energy density of 1000 W m^{-2} and the cut-off filter was used to emit wavelengths greater than 400 nm. At regular intervals, 2 mL of the solution was removed and then centrifuged, and the concentration of the model dye was determined by measuring the maximum absorption intensity. The ability the photocatalyst to degrade the dye was calculated using eqn (2):

$$\text{Degradation efficiency (\%)} = (1 - C/C_0) \times 100 \quad (2)$$

2.4.3. Seed germination. The sustainability of the photocatalyst was carried out using the treated RhB dye solution for the phytotoxicity assessment. Mung beans (*Vigna radiata*) were used to test the phytotoxicity of the untreated RhB (50 ppm) and photocatalytic-treated RhB solution. After 60 min of the photodegradation process, the photocatalytic-treated RhB solution was collected. In addition, distilled water (DW) was used as a control. Soil was put into a plastic dish containing 20 seeds of *V. radiata*, and the experiments were performed in triplicate for every condition tested. The seeds were sown in the soil and incubated at 25 °C, and then exposed to sunlight and kept in outdoor conditions. The seeds were allowed to germinate and grow for 6 d, and the seed germination was observed continuously. The number of germinated seeds was counted daily until the completion of the experiment. The germination percentage (GP%) was calculated using eqn (3):

$$\mathrm{GP}\,\% = \frac{\text{Number of seeds germinated}}{\text{Total number of seeds}} \times 100 \quad (3)$$

Next, length of the root and shoot after 6 d was measured by using the standard centimeter scale. The effect of the DW, untreated RhB solution, and treated RhB solution on the plant parameters was determined.

3. Results and characterizations

3.1. Structural and optical properties

3.1.1. X-ray diffraction. The X-ray diffraction (XRD) patterns of the synthesized photocatalysts were examined to determine their phase, purity and crystallinity. The diffraction peaks at 2θ values of 26.64, 43.94, 52.10 of PVP@CdS corresponded to the planes: (111), (222) and (311), respectively, and these were assigned to the cubic zinc blende phase of CdS (JCPDS-89-0440). Similarly, the 2θ values of the diffraction peaks at 27.21, 29, 34.96, 44.63, 52.54 of N-CQD@CdS corresponded to the diffraction from the planes (100), (101), (102), (110) and (112), respectively, and these were assigned to the hexagonal wurtzite phase (JCPDS-80-0006). The peaks at 27.90, 31.63, 36.88, 44.78 (mixed phase of 2 planes), 47.3 and 52.38 of CQD@CdS corresponded to the 2θ values of the diffraction peaks from the planes (101), (200), (102), (110), (220), (103) and (112), respectively, and these were characteristic of a mixed structure of CdS. The broadened diffraction pattern in all the samples were due to its small crystallite size. It was observed that the synthesized samples had a high crystallinity and did not contain any impurities. There were additional peaks in the XRD patterns of CQD@CdS and N-CQD@CdS which signified the presence of a limited amount of CQD in the crystal structure of the CdS photocatalyst. Similar observations were also reported by Cheng *et al.*,[58] and no distinct XRD peak was observed due to addition of the carbon dots (CDs) in the CdS nanosheets, which can be attributed to the low concentration of the CDs. Further observations from XRD spectra showed that a phase transformation has occurred from the cubic zinc blende to the wurtzite hexagonal with the addition of CQD/N-CQD. However, a mixed phase structure was attained using pure CQD, whereas using N-CQD gave a pure hexagonal phase of CdS.[62–64] This can be attributed to presence of a large amount of electronegative N^{3-} and S^{2-} atoms in the N-CQD@CdS samples, whereas CQD@CdS only has S^{2-}. It was also found that the presence of less electronegative atoms in a compound favored an hexagonal-cubic mixed phase formation due to the decrease in its nucleation rate.[49]

To further verify the mixed phase structure of CQD@CdS, selected area (electron) diffraction (SAED) patterns and *d*-spacing analysis were done and their transmission electron microscopy (TEM) images are shown in Fig. 1b and c. The SAED rings for the respective lattice planes of the wurtzite phase (110, 101, 102, 112 and 004) and the zinc blende phase (200, 220) confirmed the co-existence of both phases. Some noticeable distortions were found on the phase junction region, and these were created due

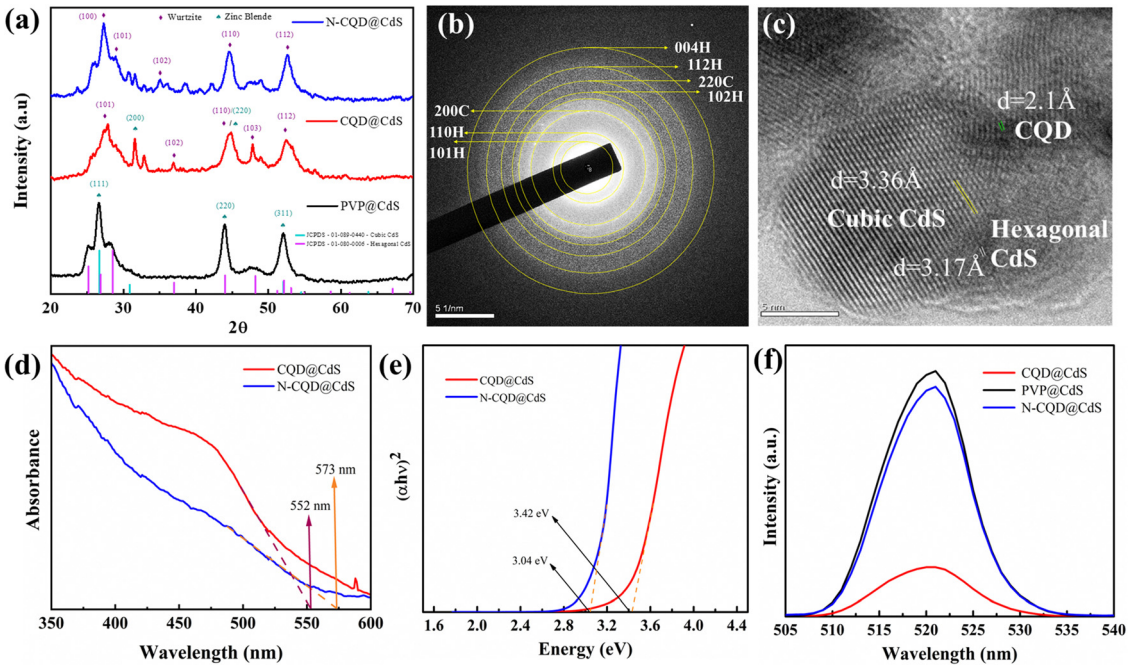

Fig. 1 Shows the diffraction pattern (a), absorbance spectra (d), Tauc plot (e) and photoluminescence spectra (f) of all the CdS samples, and the SAED (b) and TEM lattice fringes (c) of the CQD@CdS samples.

to the lattice strain and the structural defects in these nanocatalysts. The *d*-spacing for the hexagonal phase was found to be 3.17 Å and the cubic phase was 3.36 Å. The CQD doping on these mixed phase structures was also confirmed and the *d*-spacing was 2.1 Å. Also, by varying the CQD and CdS ratio there was no peak shift, whereas the intensity was decreased as shown in Fig. S8 (ESI†). These results were found to be similar with those reported in the literature Gogoi *et al.*[65] It was found that hexagonal phase of CdS promoted high stability, low charge recombination and increased the catalytic action.[66] The dominance of the hexagonal phase in any compound having a mixed phase elevated the overall photocatalytic efficiency.

The average crystal size and microstrain stress were obtained as structural parameters from the XRD data. To estimate the average crystallite size of the CdS nanostructures, the Debye–Scherrer formula was employed as shown in eqn (4):

$$D = k\lambda/\beta\mathrm{Cos}\,\theta \quad (4)$$

where k is the crystal shape constant (0.94), λ is the wavelength of the X-ray, β is the full width at half maximum, and θ = Bragg's diffraction angle. The microstrain stress was evaluated by using eqn (5):

$$\varepsilon = \beta/4\tan\theta \quad (5)$$

The dislocation density was also calculated by using eqn (6):

$$\Delta = 1/D^2 \quad (6)$$

Nanostructures often have surface defects, which are caused by dislocations, vacancies and shear strain planes. These defects can act as traps for the photoinduced charge carriers and adsorption sites. When the electrons transfer to these adsorbed sites, it can prevent the recombination of photoexcited electron–hole pairs.[67] Recent studies have shown that increasing the number of surface defects can enhance the charge separation and improve the catalytic activity.[68] From Fig. S7 (ESI†), it was observed that CQD@CdS and N-CQD@CdS had a high average strain and dislocation density, and this can be due to its mixed phase and the presence of SVs confirmed by the X-ray photoelectron spectroscopy (XPS) and energy-dispersive X-ray spectroscopy (EDAX) analyses. Thus, helping the CQD@CdS to show better H_2 evolution and better dye mineralization.

3.1.2. Fourier transform infrared spectroscopy. The FTIR spectroscopy of CQD and N-CQD is shown in Fig. S1a (ESI†). Typically, the CQDs are formed by the breakdown and condensation of large glucose molecules, that show a bending vibration of $-CH_2$ at 765 cm^{-1}. The peak at 1593 cm^{-1} in CQD is from the C=C bond which occurs due to the skeletal vibrations of the aromatic rings. The transmittance peaks at 2882 cm^{-1} and 1385 cm^{-1} correspond to the stretching vibrations of C–H. The stretching vibrations of the C=O and –OH groups were confirmed from the peaks at 996 cm^{-1}, 1142 cm^{-1} and 3350 cm^{-1}, respectively.[69] This confirmed that the synthesized CQDs are water soluble and are highly hydrophilic.

The bond interaction between PVP and CQD with CdS was studied and the results are shown in Fig. S1b (ESI†). The broad band centered at 3280 cm^{-1} was due to H–O–H bending vibrations of the water molecule. The characteristic bands located at 1654 cm^{-1}, 1409 cm^{-1} and 2882 cm^{-1} were ascribed to the C=O stretching modes, and C–H bonding of the PVP monomer. The presence of CQD on the CdS surface was

confirmed by the bands at 1440 cm^{-1} and 1044 cm^{-1} that were assigned to the C=C and C–N bonds, respectively. The occurrence of amine functional groups in the N-CQDs was confirmed by a slight peak at a wavenumber of 3117 cm^{-1}. The N-CQDs were then coordinated to the surface of CdS by these $–NH_2$ groups.[64] A detailed description of the functional groups of each sample are shown in Table S1 (ESI†).

3.1.3. UV-Vis absorbance spectroscopy. Studying the optical absorption spectrum of a material has proven to be a valuable method for determining different aspects of its band structure. In this present study, the absorbance spectra of PVP@CdS, CQD@CdS and N-CQD@CdS were determined in the wavelength range of 350–600 nm as shown in Fig. S2c (ESI†) and Fig. 1d. When the size of the semiconductor nanoparticles made of Group II–VI elements was reduced, they underwent significant changes in their optical properties, and this phenomenon is known as the quantum confinement effect.[70] The reason behind this effect was that the small size of the nanoparticles confined the movement of the electrons and holes, causing changes in their energy levels, which in turn affected the wavelength of the light they absorbed or emitted. Therefore, the optical properties of the semiconductor nanoparticles were strongly dependent on their size, shape, and composition, and can provide valuable insights into their band structures. Based on these findings, the absorbance spectra of the CdS nanocomposites were thoroughly studied. Fig. S2a and b (ESI†) shows the absorbance spectra of CQD and N-CQD. It revealed two absorption band peaks in the 200–300 nm range. The peak at 230 nm was associated with the π–π* transition of the aromatic C=C bond with sp^2 hybridization, whereas the peak at 300 nm was attributed to the n–π* transition of the carbonyl or amine groups present on the surface.[71,72] The absorption spectrum in Fig. 1d demonstrates noticeable variations in the 550–600 nm wavelength range for the CQD loaded CdS samples. The ''blue-shift'' of λ from λ = 574 nm (for standard CdS samples) to 573 and 552 nm was observed in CdS when the N-CQD and CQD were introduced, respectively. This, established that the CQD@CdS and N-CQD@CdS particles had been successfully synthesized. The observed hypsochromic shifting in the synthesized CdS nanoparticles is believed to be associated with a slight reduction in particle size, which was consistent with the XRD results. This outcome also indicated that the decrease of absorption maximum was in the order of PVP@CdS > N-CQD@CdS > CQD@CdS. Specifically, PVP@CdS exhibited the strongest absorption (Fig. S2c, ESI†) in the visible light range at 574 nm. Whereas the N-CQD@CdS showed an absorption maximum at 573 nm, and the CQD@CdS showed a maximum at 552 nm as shown in Fig. 1d. Further, the corresponding optical band gap for the CdS samples were calculated and are shown in Table 1 and their respective Tauc plots are shown in Fig. 1e. The PVP@CdS possesses the smaller band gap of whereas the N-CQD@CdS and CQD@CdS have wide band gaps. The presence of CQD did not have a significant change in optical properties[73] and this was also confirmed from other results reported in the literature that showed similar results to ours.[65,74]

Table 1 Shows the band gaps and sizes of the synthesized CdS samples

Sample name	Band gap (eV)	Absorption maxima (nm)	Size (nm)
PVP@CdS	2.160	574	37
CQD@CdS	2.223	554	24
N-CQD@CdS	2.175	570	33

The average particle size (R) of the CdS nanoparticles was estimated using the Brus eqn (7):

$$E_g = E + h^2/8R^2\,[1/(m_{e^*}) + 1/m_{h^*}] - 1.8e^2/\varepsilon R \qquad (7)$$

where E_g is the band gap of the synthesized QDs, E is the bulk band gap of CdS (2.4 eV), R is the radius of the particle, m_e is the effective mass of the electron (for CdS, it is 0.19 m_o), m_h is the effective mass of the hole (for CdS, it is 0.8 m_o), ε is the dielectric constant of the material, and h is Planck's constant. The band gap was calculated using eqn (8):

$$E_g = 1240/\lambda \qquad (8)$$

where, E_g is the band gap of CdS, and λ is the wavelength of the absorption maximum for CdS. The energy band gap (E_g) and average particle size values are shown in Table 1, and these values were similar to the results obtained with TEM and XRD, which are discussed in the previous sections.

3.1.4. Photoluminescence (PL). Fig. 1f shows the down-converted PL spectrum of CQD@CdS. The spectral nature of the CQD derived from the glucose was evident from the excitation wavelength-dependent emission. The CdS samples were excited at 340 nm and an emission peak was observed at 520 nm. The gradual decrease in intensity for the CQD@CdS was attributed to the surface functional moieties and the degree of surface oxidation. An increase in the number of surface energy traps lead to a higher number of excitons being trapped, resulting in a decrease in the recombination rate.[75,76] This proved that the CQD@CdS sample possessed lowest charge carrier diffusion rate when compared to those of PVP@CdS and N-CQD@CdS. The PL intensity of the peaks obtained for PVP@CdS and N-CQD@CdS were very close to each other, which can be also justified from nearly same H_2 generation performance of these particles discussed in later sections.

3.2. Morphological properties

3.2.1. Scanning electron microscopy and transmission electron microscopy. The morphologies of the prepared nanocatalysts were studied using scanning electron microscopy (SEM) and TEM image analysis. The SEM and TEM images of CQD@CdS are shown in Fig. 2a and b, respectively. The synthesized samples had a spherical like structure with an average size of ~23 nm. The SEM images of PVP@CdS and N-CQD@CdS are shown in Fig. S3a, b (ESI†) and Fig. 1c and Fig. S3d (ESI†), respectively. The TEM images of CQD@CdS and N-CQD@CdS revealed lattice fringes and this was assigned to the hexagonal and cubic planes of CdS. The interlayer lattice spacing (d) of CQD@CdS was found to be 3.36 Å for the cubic phase and 3.17 Å for the hexagonal phase of CQD@CdS, and this was consistent with other results available in the literature.[77]

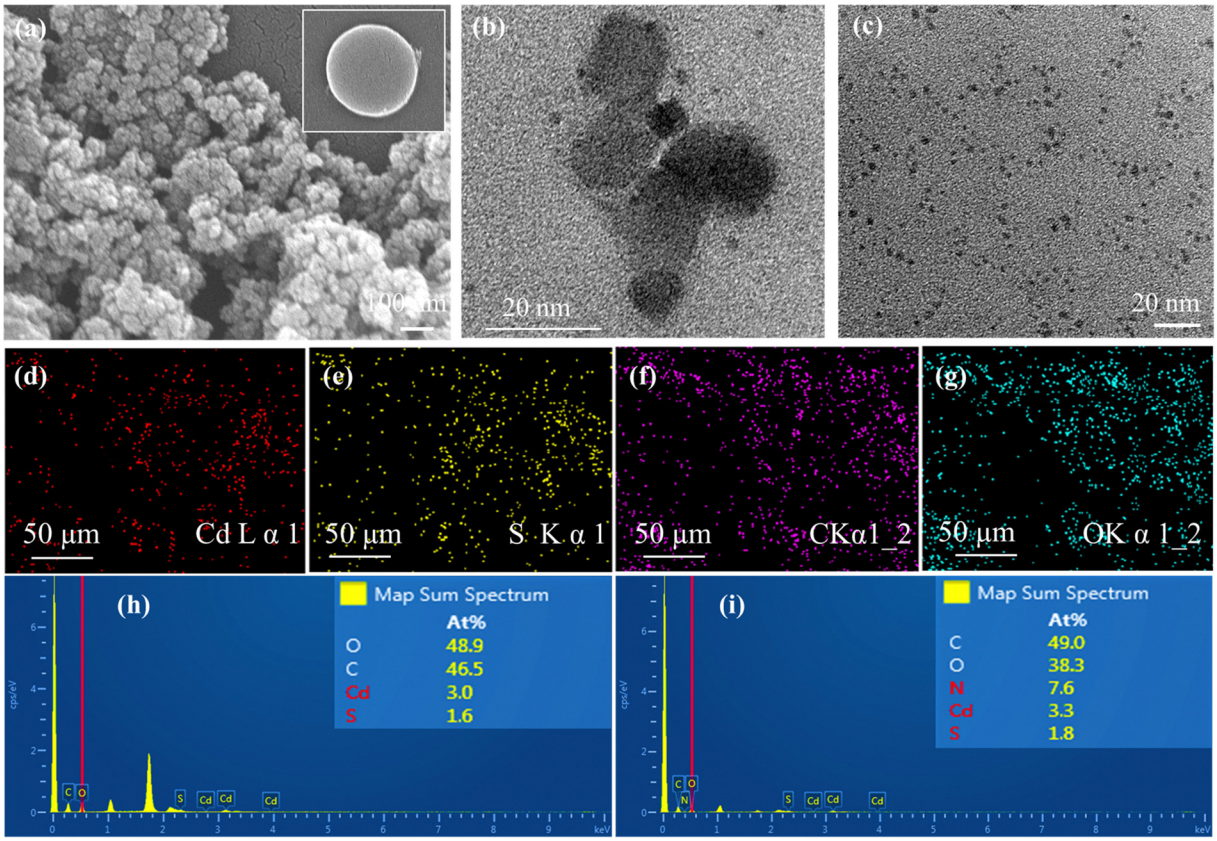

Fig. 2 This shows (a) SEM and (b) TEM images of CQD@CdS, (c) the SEM image of CQD. (d)–(g) elemental mapping, and the EDAX spectra of (h) CQD@CdS and (i) N-CQD@CdS.

Further detailed analysis of the SAED rings is found in Section 3.1.1 X-ray diffraction. Because of the small size and amorphous nature of the CQDs, it was not able to observe them clearly in the TEM image Fig. 2b.[78] However, the individual image of the CQD in Fig. 2c showed that their size was in the order of ~3 nm and the particle size distribution is shown in Fig. S3c (ESI†). No significant change in the morphology of the CdS was observed with the introduction of the CQD surface. However, with the introduction of the CQDs it reduced the agglomeration of CdS. The presence of CQD on the CdS was confirmed by the elemental mapping images of CQD@CdS and N-CQD@CdS shown in Fig. 2d–g and Fig. S3e–i (ESI†), respectively. It was observed that the percentage of sulfur was comparatively low compared to that of cadmium in the synthesized samples, and to verify this EDAX analysis was performed. Fig. 2h and i display the EDAX of the CQD@CdS and N-CQD@CdS, respectively. The elemental composition was C, Cd, O, and S in CQD@CdS, and C, Cd, N, O and S in the N-CQD@CdS samples with a tolerable impurity phase. The EDAX profile shows the presence of a small amount of sulfur which corresponds with the elemental mapping results. This could be due to the creation of sulfur vacancies, and these act as trap sites that reduce the electron–hole recombination providing a longer lifetime. A detailed explanation of this is given in later sections.

3.2.2. BET surface area. The BET surface area and the N_2 adsorption–desorption isotherms of samples are shown in Fig. 3a–c. These plots reveal, an increase in surface area and the presence of type IV isotherms, indicating that the CQD modifications alter the pore structure of the CdS. The presence of these carbonaceous compounds on the surface of CdS, enhanced the active surface area for adsorption, and was likely be due to the decrease in agglomeration of the particles that is evident in the SEM and TEM images. The total surface area for CQD@CdS was 32 m^2 g^{-1}, whereas for bare CdS it was 0.8 m^2 g^{-1}, and this could be due to their larger particle size (Fig. 3d) that reduced their surface area. Furthermore, addition of nitrogen in CQDs, can occupy or block the active sites on the carbon surfaces. These active sites are responsible for gas adsorption in the BET. When these sites were occupied with other elements, the available surface area for adsorption decreased, leading to a reduction in the overall surface area of the sample. The CdS is primarily composed of a mesoporous structure whereas the CQD exhibited the presence of multimodal micropores and mesopores.[79] This microporous and mesoporous structural design which has a larger surface area may have a significant impact on the adsorption and photocatalytic processes.

3.3. X-ray photoelectron spectroscopy (XPS)

The surface composition and oxidation states of the elements in the synthesized samples were confirmed by XPS analysis and the results are shown in Fig. 4. The full survey scans for the

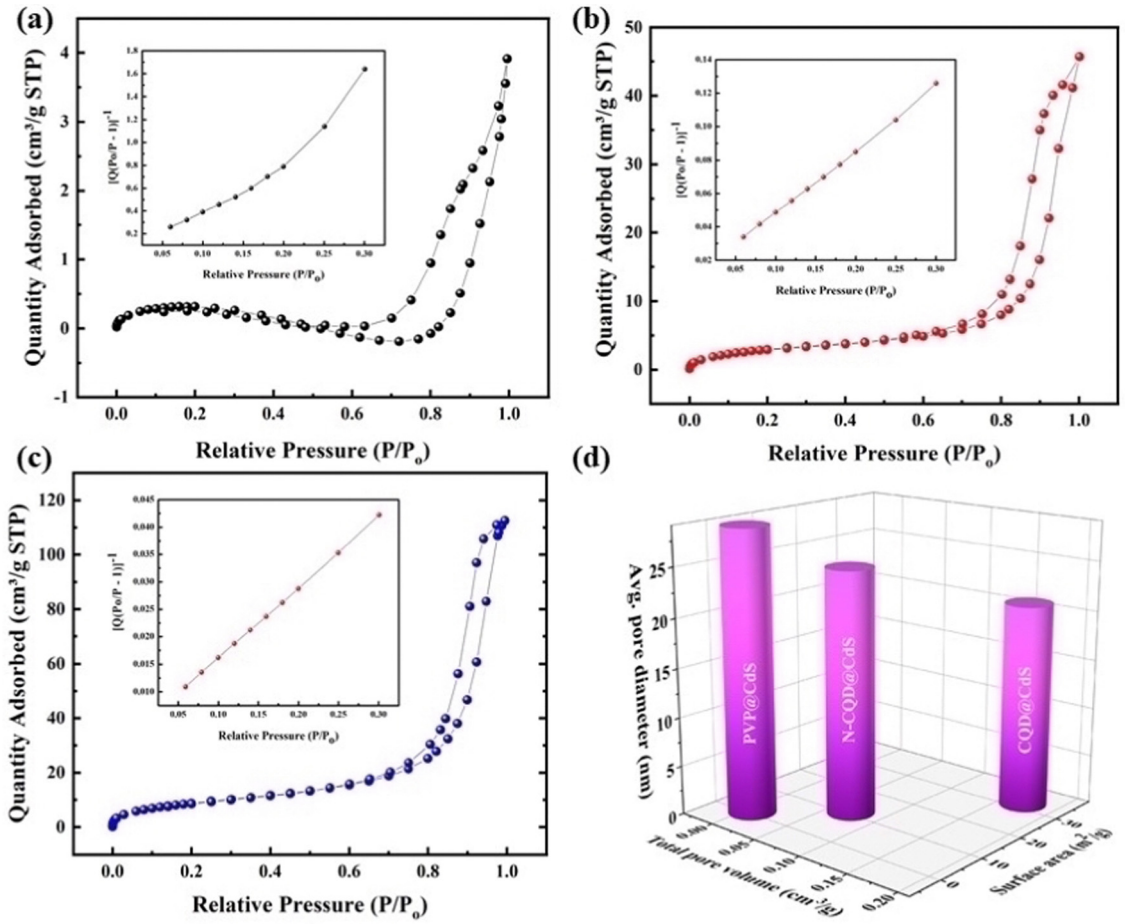

Fig. 3 The BET absorption–desorption isotherms (a)–(c), and the pore size distribution and surface area (d) of the CdS sample.

PVP@CdS, CQD@CdS and N-CQD@CdS spectra confirmed the presence of the elemental components: C, Cd, N, and S (Fig. S4, ESI†). The complete analysis of the high-resolution C 1s core level spectrum revealed intricate details, featuring distinct peaks indicative of various carbon functional groups. In particular, for PVP@CdS, the peaks centered at 284.39 eV, 286.09 eV, 287.95 eV (Fig. 4c) corresponded to –C–C/–C═C, –C–O, and –C═O, respectively. Similar functional groups were observed for CQD@CdS (284.51 eV, 285.85 eV, 287.36 eV, Fig. 4f) and N-CQD@CdS (284.38 eV, 285.36 eV, 287.01 eV, Fig. 4i). The full survey spectrum highlights a comparatively small carbon peak intensity in PVP@CdS, which confirmed the presence of CQD in later samples. The Cd 3d spectra (Fig. 4a, d and g) distinctly show the presence of two major peaks signifying the Cd^{2+} oxidation states in the samples.[80] Furthermore, the deconvolution of the S 2p spectrum revealed doublet peaks for each sample: PVP@CdS (160.92 eV and 162.08 eV, Fig. 4b), CQD@CdS (160.49 eV and 161.68 eV, Fig. 4e) and N-CQD@CdS (160.49 eV and 161.61 eV, Fig. 4h) which were associated with S $2p_{1/2}$ and S $2p_{3/2}$, respectively.

The Cd 3d and S 2p spectra of CQD@CdS and N-CQD@CdS showed a peak shift towards lower binding energies, when compared to bare PVP@CdS. This shift of energy levels indicated an enhancement in the electron density on CdS, which suggested there was a significant chemical interaction between the CQD and the CdS.[63] The elemental analysis data are summarized in Table S4 (ESI†). Interestingly, the atomic percentage of sulfur in CdS became smaller with the use of CQD, when compared to that of bare PVP@CdS. This result indicated that the CQD supports the SV, thereby increasing the cadmium population. According to previous reports, the electron trap sites were identified in between the energy bands of 0.63–0.7 eV, *i.e.*, below the conduction band (CB) of the bulk CdS, and these trap states in the crystal are assigned to SVs. Furthermore, the change in the Cd peak also supported the existence of a Cd surface with SVs[81] and a decrease in the electronegative S atoms because of the lower binding energy shift occurred.[82] This confirmed the presence of CdS with a deficiency in the S concentration that helped to increase the photocatalytic action.

Further, to confirm the XPS results for the SVs, electron paramagnetic resonance (EPR) analysis was performed as shown in Fig. S9 (ESI†). All the CdS samples showed resonance signals at $g = 0.19$. The weak signal for N-CQD@CdS prepared by a hydrothermal method involved low SVs. However, when the CQD was used instead of N-CQD, the EPR response also changed significantly. These results were also similar to the XPS elemental results shown in Table S4 (ESI†). Also, the SVs

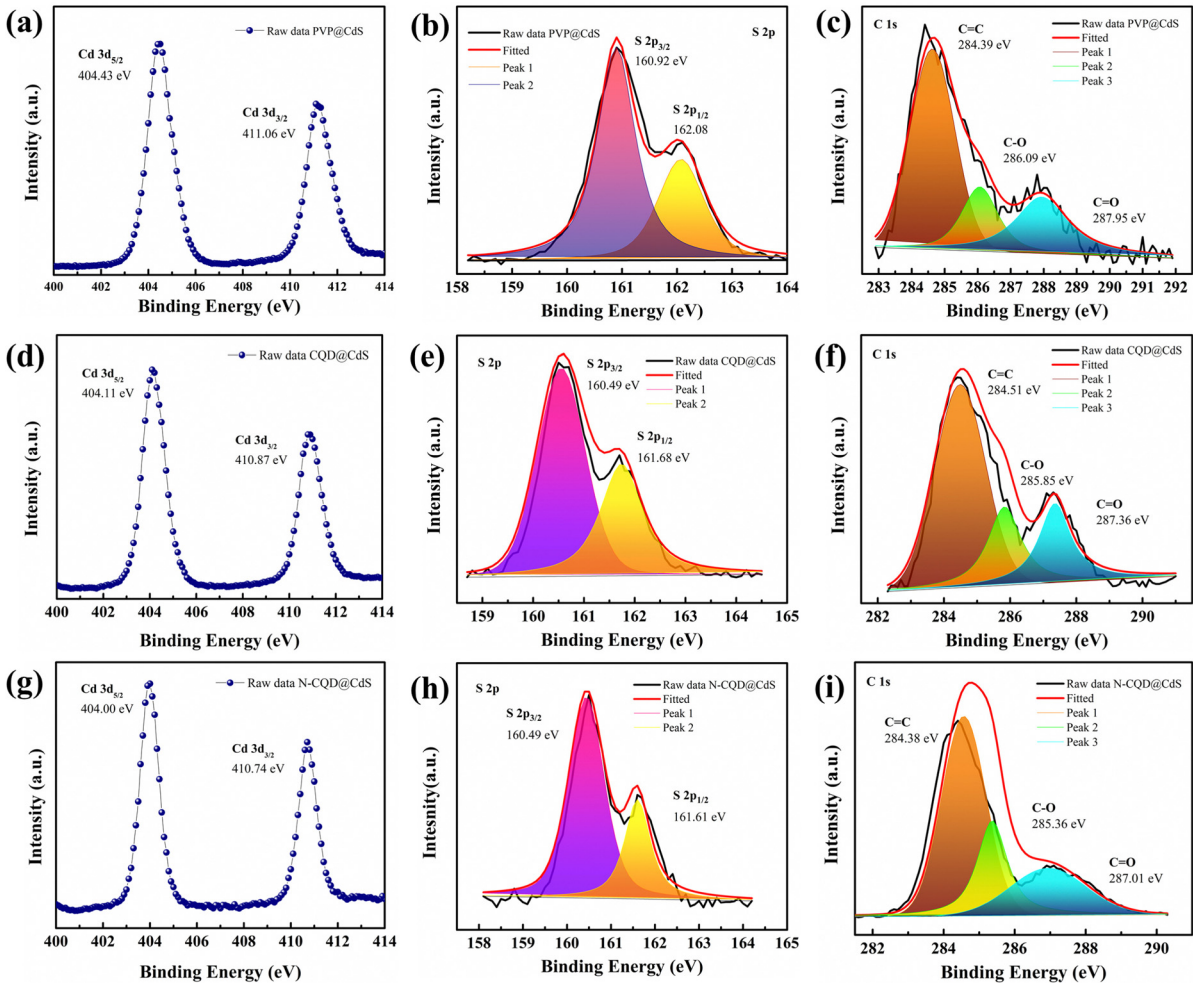

Fig. 4 The XPS spectra of the PVP@CdS, CQD@CdS and N-CQD@CdS samples with their respective (a), (d) and (g) Cd 3d, (b), (e) and (h) S 2p, and (c), (f) and (i) C 1s elements.

can enhance the free charge carrier, expose more active sites, and promote the mobility of the electrolyte ions, which was favorable for electrochemical activity.

4. Photocatalytic performance

4.1. Rhodamine B dye degradation

The assessment of photocatalytic efficiency for the CQD@CdS material was carried out using a comparative analysis with N-CQD@CdS, with RhB dye as the model target molecule.[63] The degradation of RhB under visible light illumination was studied using a blank experiment, which showed minimal degradation. To assess the degradation efficiency of the photocatalysts, 25 mg of each catalyst was used for a 50 mg L^{-1} concentration of the RhB dye, and the decrease of the absorption peak was monitored under visible light conditions. The results in Fig. 5c indicate that the N-CQD@CdS achieved a degradation efficiency of 52%, whereas the CQD@CdS resulted in 97% degradation of RhB within 60 min. Fig. 5a and b illustrate the decline in RhB dye concentration over time periods of 115 min and 60 min for N-CQD@CdS and CQD@CdS, respectively. The N-CQD@CdS reached its saturation point after half of the time period, whereas the CQD@CdS continued to degrade the dye because of the strong adsorption of toxic components on catalyst surface causing the catalyst to be completely oxidized.[83] To understand the kinetics and mechanism of the RhB dye mineralization with optimized catalytic loading, Langmuir–Hinshelwood and pseudo-second order kinetic models were utilized. The Langmuir–Hinshelwood model, which is also known as a pseudo-first order model is given by eqn (9):

$$\ln(C_t/C_0) = -K_{app}t \quad (9)$$

where C_0 is the initial concentration, and C_t is the final concentration. The pseudo-second order kinetics were calculated using eqn (10):

$$(1/C_t) - (1/C_0) = K_{app}t \quad (10)$$

The linear fit between $\ln(1/C_t)$ against t is shown in Fig. 5d. Further, many previous reports have been done, and these show that with an increased amount of the pollutant, the degradation efficiency decreased which was due to a smaller

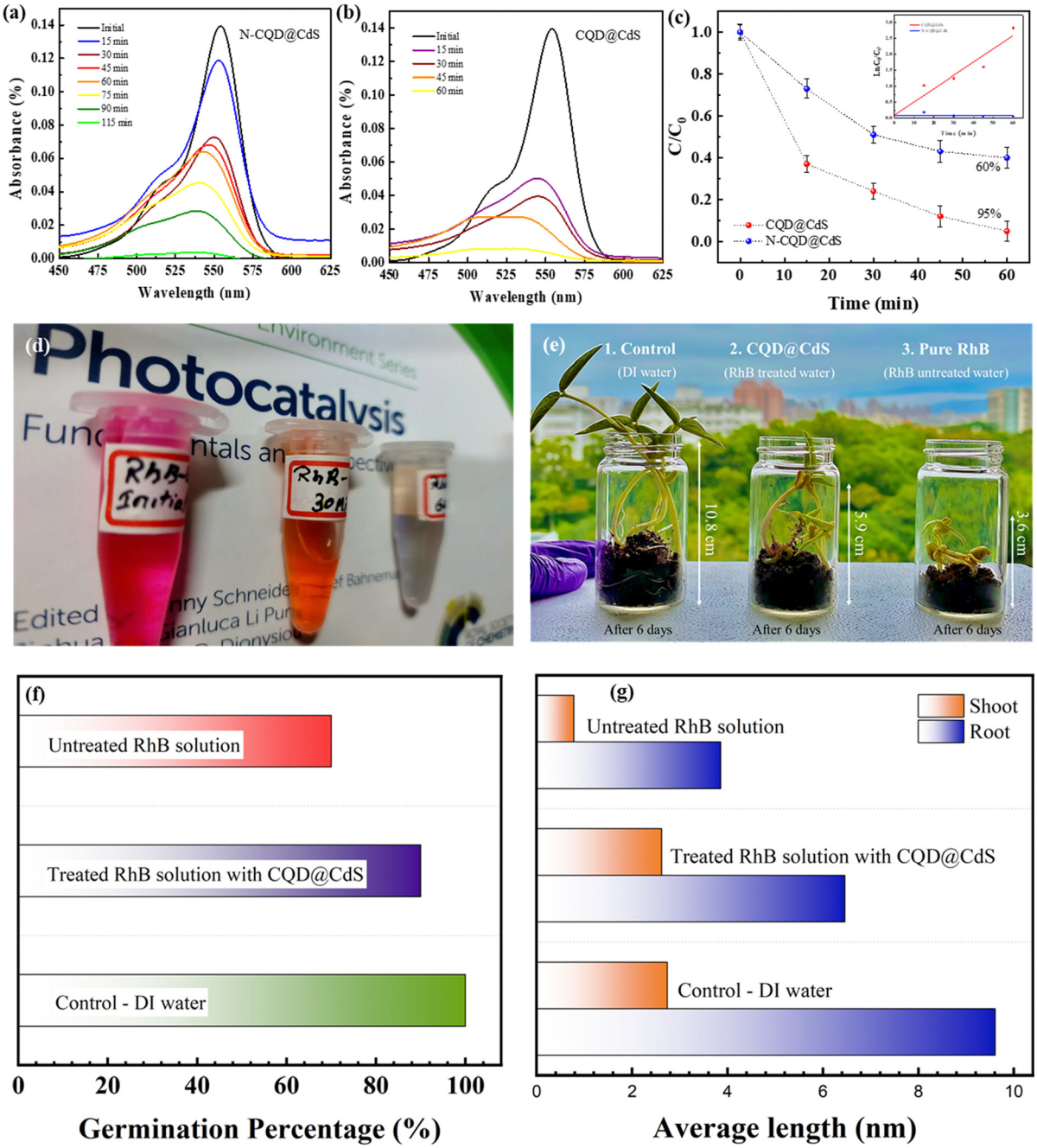

Fig. 5 The Rhodamine B degradation absorbance spectra by N-CQD@CdS (a), and CQD@CdS samples (b). Dye degradation efficiency and pseudo-second order kinetic plot (c), change of dye over a 60 min time period (d), *Vigna radiata* growth rate profile with different sources of water (e) and growth rate (f), roots and shoots lengths (g).

number of active sites being available on the photocatalyst, which limited the hydroxyl and superoxide anion radicals generated.[62]

A comparative analysis of the degradation of the RhB dye using other reported materials is shown in Table S2 (ESI†). Bhavsar *et al.*, synthesized activated carbon loaded CdS nanoflowers using a hydrothermal method that showed a degradation of 95% of RhB in 295 minutes.[79] Similarly, Fan *et al.*, reported a CdS heterostructure photocatalyst made by combining it with nonporous g-C_3N_4 nanoparticles and their combined effort degraded the RhB by 88.2% in 90 min.[84] A unique Y-shaped CQD embedded on CdS nanorods was reported by Moniruzzaman *et al.*, in which they successfully degraded 98% of RhB dye in 45 min.[85] This higher efficiency was attributed to the Y-shape of the CQD that helped to increase the visible light absorption. In the research here, the CQD decorated the CdS nanostructures with surface defects which were synthesized by a hydrothermal process. Further, the dye degradation efficiency was checked with RhB, and degradation of 97% was achieved in 60 min. This improvement was attributed to the larger surface

area of CdS which facilitated the superior adsorption of the dye. In addition, there was the presence of CQD with more active sites with functional groups (–COOH, –OH, $–NO_2$) that interacted with the RhB molecules. This also increased the lifetime of the electron–hole charge carriers and enhanced their separation (Fig. 1f). Overall, the synergistic effects of adsorption and photocatalysis contributed to the improved degradation of RhB by the CQD@CdS composites.[51,52] The ameliorated disintegration of RhB molecules by CQD@CdS composites was the collaborative outcome of adsorption and photocatalysis.

Further, a shift of absorbance was observed as the dye concentration gradually decreased (Fig. 5a and b). Similar findings were reported by Ahsaine *et al.*,[86] who noted two possible photodegradation pathways for RhB: the cleavage of the complete conjugated chromophore and *N*-deethylation. If the degradation of RhB involves the cleavage of a conjugated chromophore, the peak intensity decreases while the peak position remains constant. However, if it follows the *N*-deethylation photodegradation pathway, the peak position gradually shifts to a lower wavelength (blue shift). In our study, it was observed that photodegradation of RhB follows a *N*-deethylation pathway, as shown by the main peak position shifting from 554 nm to 498 nm. The possible mechanism for this is shown in Fig. S10 (ESI†).

Further, the phytotoxicity experiments were carried out to evaluate the potential use of the pre-treated aqueous solution in the irrigation field, as well as the environmental impact of the release of the degrading solution. In fact, this technique can alleviate the burden of excessive underground water use, while encouraging the use of treated water to irrigate golf courses, parks, and gardens. Fig. 5e represents the phytotoxicity of untreated and treated RhB and DI solutions using a seed germination assay. The stubborn nature of RhB and DI was reflected in the fact that the untreated solution strongly inhibited seed germination in mung bean seeds (*V. radiata*) when compared to use of treated and distilled water solutions over 72 h. It was observed, that the pollutant molecule in the presence of a dye solution influenced plant length and seed germination. In seed germination, the percentage value when compared to control DI water (100%), and the RhB solution shows 70% and 82.2% degradation, respectively (Fig. 5f). These results clearly show that the toxicity of the degraded dye solution was within an acceptable range. Another significant length profiling study was also conducted (Fig. 5g), and this study also showed that the degraded dye solution was less toxic. These findings suggested that the photocatalytic degradation of RhB and DI aqueous solutions can reduce phytotoxicity. Hence, seed germination might be a suitable for the reuse of treated water.

4.2. Hydrogen generation

The overall water splitting (OWS) hydrogen generation of the developed photocatalyst were examined using a solar simulator with visible light irradiation ($\lambda \geq 420$ nm). The photocatalysts were suspended in a solvent mixture containing TEA, MeOH together with DI water (1 : 1 : 10) and the evolved H_2 was measured using a gas chromatography workstation. The TEA acted as a sacrificial electron donor and the MeOH was used to reduce the phase segregation between TEA and water.[87] Fig. 6a illustrates the sustained H_2 production exhibited by all three photocatalysts over a period of 10 h, with their performance in the sequence of CQD@CdS > PVP@CdS-S > N-CQD@CdS. Remarkably, the CQD@CdS composites manifested a superior H_2 evolution (3928 μmol g^{-1} h^{-1}), which was nearly four-fold higher than that of the bare PVP@CdS (965 μmol g^{-1} h^{-1}). This enhancement in H_2 generation rate performance was attributed to the presence of CQD on the CdS surface as shown in Fig. 6b. However, a conspicuous decline in efficiency was observed in nitrogen doped CQD CdS samples, and a HER of 907 μmol g^{-1} h^{-1} was recorded. This can be attributed to the nitrogen impeding the active sites on the CQD surface, consequently diminishing its effective surface area (Fig. 3d), and this resulted in higher electron–hole recombination (Fig. 1f).

Furthermore, the evaluation of the optimal loading of CQD (1 mL, 2 mL and 3 mL) on the CdS surface is shown in Fig. 6c. When 1 mL or 2 mL of CQD was used it showed a reduced H_2 generation activity compared to when 3 mL of CQD was used. Conversely, an increase in the amount CQD, again resulted in a decrease in H_2 generation as it can lead to blocking of the CdS surface. When the CQD amount was low, it was not able to absorb sufficient visible light for CdS. Therefore, maintaining an optimal amount of CQD is crucial to achieving the maximum enhancement in the photocatalytic performance. The AQY of all the three developed photocatalysts was calculated (eqn (1)), and the values were: PVP@CdS – 2.3%, N-CQD@CdS – 2.2% and CQD@CdS – 20.98%. The observed high AQY of CQD@CdS was due to the higher H_2 evolution rate compared to other photocatalyst. These CQDs not only lower the overpotential for H_2 generation in the CQD@CdS systems, but also serve as a consistent and easily approachable electron acceptor. Moreover, the CQD have a π-conjugated structure and oxygenated functional groups in its surface, which can easily interact with the CdS matrix.[88] This interaction serves as an electronic buffer, enabling the continuous supply of electrons to the adjacent CdS semiconductor with appropriate band edge positioning, leading to H_2 generation from H^+.

Catalyst loading and reusability. To find the optimized catalyst dosage, water splitting was carried out using 25 mg and 50 mg of CQD@CdS and the H_2 generation rates over 10 h were 39 287 μmol g^{-1} and 80 466 μmol g^{-1}, respectively, (Fig. 6d). At higher concentrations of photocatalyst, the catalytic system became turbid and this impeded the light irradiation.[89] The reusability of the photocatalyst developed was examined using three consecutive cycles up to 20 h (Fig. S5, ESI†). Also, photocurrent analysis (Fig. S6, ESI†) of the CQD@CdS showed the long-term stability due to the CQD loading. It was observed that the H_2 evolution remained almost constant for the first two cycles but was reduced in the third cycle, and this was possibly due to the oxidation of the radical scavenger during the redox reaction. Moreover, to verify the stability of the CQD@CdS, we measured the Cd^{2+} concentrations in the reaction solutions using ICP-MS and the results for this are shown in Table S5 (ESI†). An obvious increase of Cd^{2+} concentration was observed for PVP@CdS. However, in CQD@CdS, the concentration of

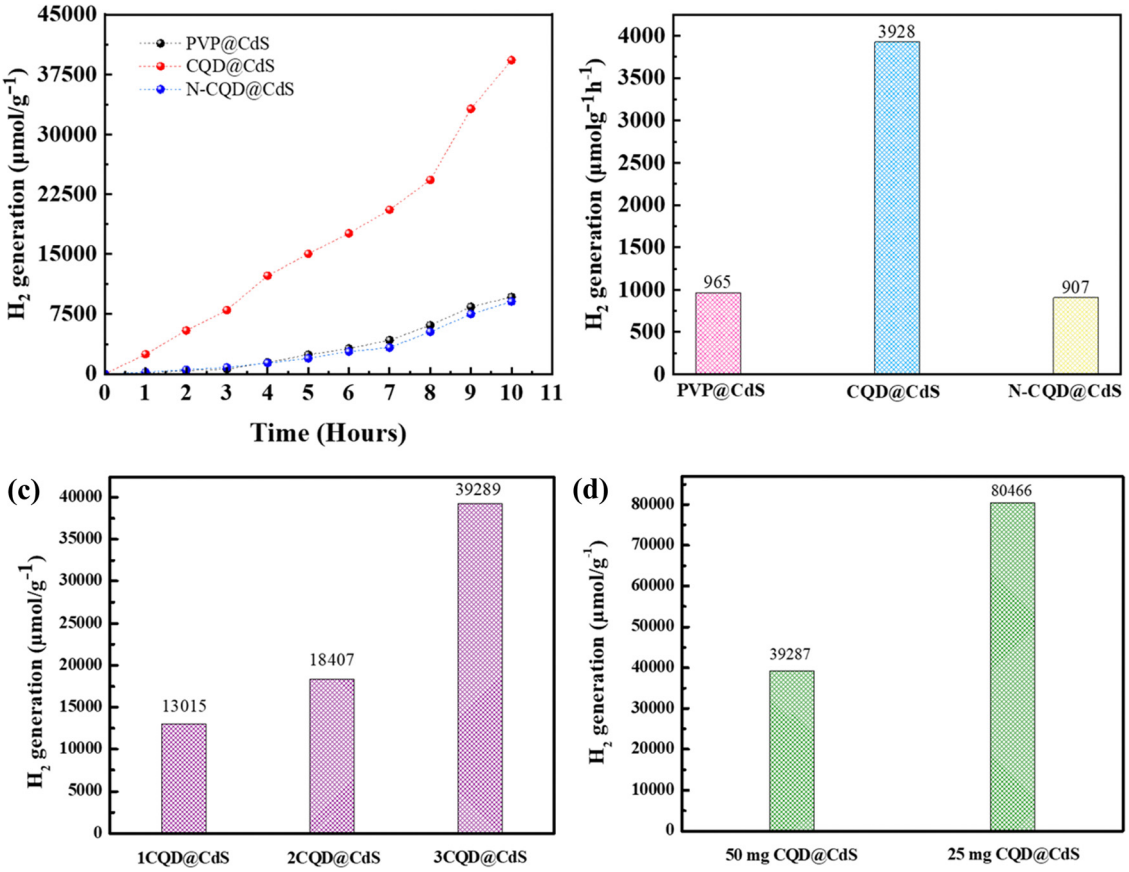

Fig. 6 The time dependent photocatalytic hydrogen generation (a), the average hydrogen generation rate over 10 h by all the CdS samples (b). The hydrogen generation rate with varying ratios of the amounts of CQD (c), and the amounts of the CQD@CdS photocatalyst (d), used for reactions.

Cd^{2+} was still low which supported its ability to hinder photocorrosion.

Seawater splitting. The CQD@CdS photocatalyst was further used for water splitting from seawater. The seawater was collected from Nanliao beach near Hsinchu City, Taiwan (24.8483°N, 120.9303°E). Prior to the experimentation, basic filtration was done using filter paper followed by 200-μm filters to separate the unwanted sand particles. The photocatalyst (25 mg) was suspended in solvent containing TEA, MeOH and purified seawater (1 : 1 : 10). A 1.5G solar simulator with a cut-off filter of $\lambda > 420$ nm was used as visible light source. The H_2 evolution was monitored continuously every hour for 10 h (Fig. 7a) and the average H_2 generation rates are shown in (Fig. 7b). Similar to the H_2 evolution activity in DI water, also the trend here remained the same in the order of CQD@CdS > PVP@CdS > N-CQD@CdS. However, a decrease in the H_2 generation rate could be seen in seawater. This was due to presence of additional salts and ions that reduced the charge carrier mobility. However, the catalyst developed showed a superior H_2 generation rate compared to others reported in the literature. This shows that the use of CQD on the CdS surface together with its mixed phase structure and presence of SVs enhanced the stability of the photocatalyst.

To elucidate the governing effect of CQD and N-CQD on photocatalytic H_2 generation of CdS electrical impedance spectroscopy (EIS), Fig. 7c) and the Mott–Schottky (M–S, Fig. 7d) energy level diagram was studied. The EIS spectra of bare PVP@CdS, CQD@CdS and N-CQD@CdS under light irradiation are shown in Fig. 7c. The arc radius in the EIS plot represents the charge separation and transport resistance between the water and the photoelectrode. The arc radius of CQD@CdS was reduced when compared to those of N-CQD@CdS and bare PVP@CdS, that confirms their better, faster charge transport kinetics and which can be also seen in the photocurrent results (Fig. S6, ESI†) and the PL observations (Fig. 1f). The CQD@CdS shows the lowest resistance among all the developed photocatalysts that support its superior hydrogen generation activity. As is already known, resistance and conductivity are inversely proportional to each other, and the lower resistance of CQD@CdS signifies the increase in electrical conductivity which was due to the CQD electron acceptor on its surface.

The M–S plots of all the CdS samples were determined in a 0.2 M aqueous solution of Na_2SO_4 using eqn (11). From these plots, the flat band potential was calculated as the intersection point of the tangent line of the M–S curves and the *x*-axis (Fig. 7d). The flat band potentials of the samples were estimated to be −0.236 and 0.0621 *vs.* SCE for CQD@CdS and N-CQD@CdS, respectively. For efficient photocatalysis, the CB of CdS should more negative than its flat band potential, thus

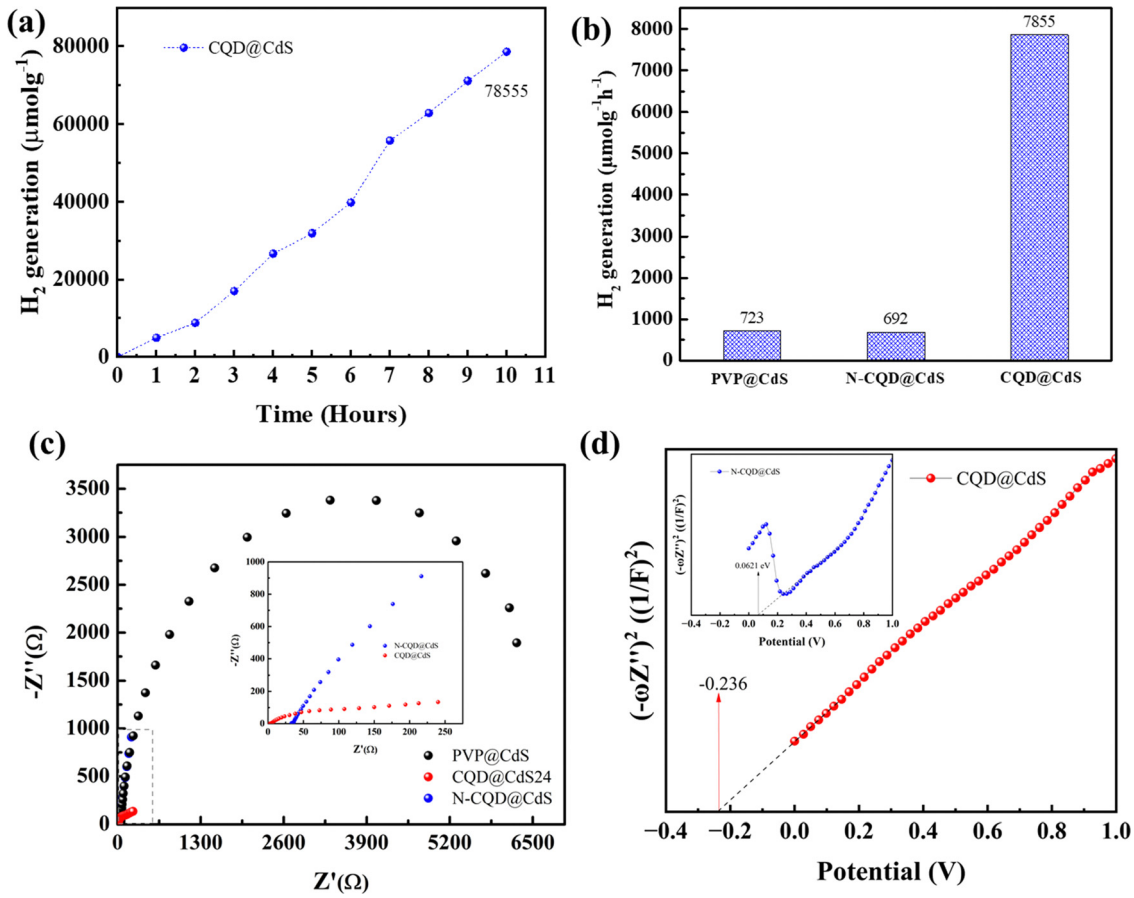

Fig. 7 Hydrogen generation (a) using seawater with CQD@CdS for 10 hours. A comparison of the hydrogen generation rate using seawater (b), EIS spectra (c) and Mott–Schottky plot (d) for all the CdS samples.

Table 2 Shows the band structure parameters such as E_f, E_g, E_{CB} and E_{VB} of the CdS samples

Sample	E_g (eV)	E_{FB} (eV)	E_{CB} (eV)	E_{VB} (eV)
CQD@CdS	2.26	−0.236	0.004	2.264
N-CQD@CdS	2.20	0.0621	0.2337	2.433

the final CB potential was converted to potential corresponding to a normal hydrogen electrode (E_{NHE}) using eqn (12) as shown in Table 2 and Scheme 1. The obtained E_{CB} values for CQD@CdS and N-CQD@CdS24 were 0.004 and 0.2337 *vs.* NHE, respectively.

$$1/C^2 = 2\,(N_D e\varepsilon\varepsilon_0)^{-1}\cdot(E - E_{FB} - kT/e) \quad (11)$$

where C is the capacitance of the space charge region, N_D is the charge carrier concentration, e is the electron charge, ε is dielectric constant, ε_0 is the vacuum permittivity, E is electrode applied potential, E_{FB} is the flat band potential, k is Boltzmann constant and T is the absolute temperature.

$$E_{NHE} = E_{SCE} + 0.24\ \text{V} \quad (12)$$

$$E_{CB} = E_{VB} - E_g \quad (13)$$

5. Discussion

The photo-corrosion of CdS occurs mainly due to the oxidation of the sulfide ions by photogenerated holes as shown in eqn (14):

$$CdS + 2h_{VB}^{+} \rightarrow Cd^{2+} + S \quad (14)$$

Tang *et al.*,[90] demonstrated the curbing of the CdS photo-corrosion by applying an amorphous carbon layer. They also examined photodegradation and noted that the fortification of CdS in the presence of CQD, lead to an increase in the photocatalytic efficacy. Similarly, Zhu *et al.*, synthesized a stable photocatalyst using carbon dots on CdS nanoparticles that generated an H_2 rate of 2.55 μmol g^{-1} h^{-1} in absence of a SRs.[58] Zero-dimensional carbon dots and a one-dimensional CdS nanowire heterostructure were reported by Chen *et al.*,[13] which showed an H_2 activity of 1633 μmol g^{-1}. Zhu *et al.*,[56] revealed the shape dependent photocatalytic H_2 generation of the CdS nanostructures with CDs loaded on it. The study showed that the CDs/CdS nanosheets showed the highest H_2 generation rate of 260 μmol g^{-1} h^{-1}. Previously carbon loaded CdS nanostructures have been reported for use in H_2 generation however, the efficiency was still found to be low. In this research, the CQD@CdS showed superior H_2 generation rate of

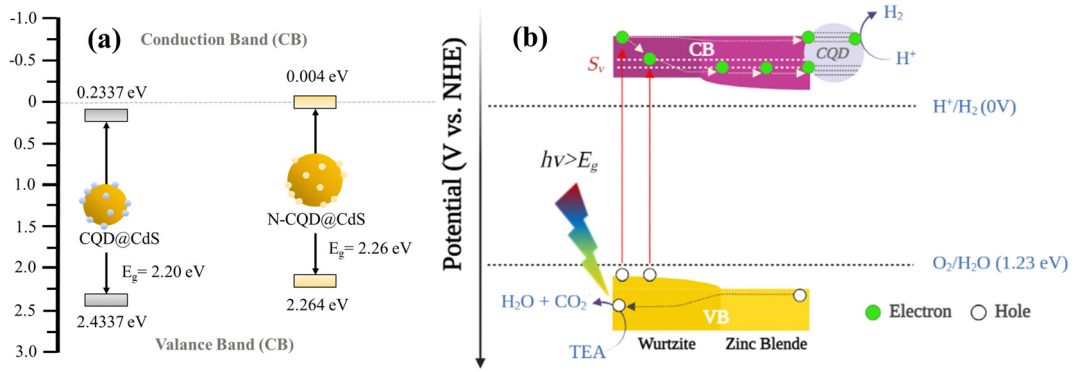

Scheme 2 The band positions of CQD@CdS and N-CQD@CdS photocatalyst (a). The photocatalytic hydrogen generation mechanism (b) for phase engineered, sulfur vacancy enriched, and CQD loaded CdS nanostructures.

8046 μmol g^{-1} h^{-1}. This was due to CdS having mixed phase structure with SVs that help in increasing the catalytic reaction. Also, the CQD on the surface of CdS acts to capture electrons from the CB of CdS and shields CdS from reactive species, particularly OH radicals/intermediate species S^- to S^{2-}. In addition, holes were captured by SR which prevents the photo-corrosion of CQD@CdS.[91] A comparison has been shown in Table S3 (ESI†).

Based on the previously mentioned findings, a feasible mechanism for the water splitting action of the CQD@CdS nanocatalysts using a visible light source is proposed in Scheme 2. Upon exposure to light, on the surface of catalyst it excites the electrons to move from the valence band (VB) to the CB leaving holes in the VB of the mixed phase CdS. Usually, these electron–hole pairs have a tendency to recombine with each other. However, due to the phase junction created between the cubic and hexagonal phases, which serves as an energy transition area to minimize energy loss and generates an internal electric field that separates the electrons and holes. These distinct band structures of phases cause the electrons to migrate from the hexagonal to the cubic phase (lower CB edge) and the holes move towards the hexagonal phase (higher VB edge).[50] Here some of the electrons get trapped in defect states (S_v) created due to SVs that reduce the probability of the electrons and holes recombining.[92] Because the CQDs are a great source for electron acceptors,[74] they attract electrons from these trap states that reduce the H^+ ions to produce H_2 gas. Furthermore, the holes in the VB reacts with TEA to form H_2O and CO_2.

In some cases it has been observed that the CQDs loading increases the absorption spectrum of the material thereby increasing the catalytic efficiency.[93] However, in the present study there has been no significant change in absorbance observed (Fig. 1d) with the introduction of CQD, and this indicates the role of the CQD in catalytic system. Here, CQD did not behave as a photosensitizer, instead it acted as a buffer zone to store electrons, thus supporting the photoinduced charge separation[94] and giving an outstanding HER performance.[58]

A sustainable way for the production of green H_2 was evaluated in this work. The present renewable H_2 generation systems pricing is at least two-fold more expensive than H_2 generated from fossil fuels. This research provides potential insights that could decrease electrolyzer costs, replaces the traditional Pt/Ir catalyst, and adopts a new generation of cost-effective carbon-semiconductor catalysts for superior H_2 evolution activity. Until today, most work with "renewable H_2" has focused on using clean water, however, we have successfully demonstrated utilization of seawater with minimum loss in H_2 evolution rate. It is expected that further understanding of the chemistry of these technologies may bring solutions to address the concerns of water issues in H_2 production in near future.

Conclusion

In summary, carbon quantum dots as an efficient cocatalyst have been used with cadmium sulfide nanoparticles which form an effective photocatalyst for hydrogen generation and water treatment. The CQD coupled with CdS exhibited an excellent hydrogen generation rate of 80 450 μmol g^{-1} and Rhodamine B dye degradation was 97% in 60 min. This was due to synergistic effect of the mixed phase, sulfur vacancies and the porous structure of CQD@CdS. The CQD not only successfully separated the photoinduced charge carriers but it also helped in increasing the lifetime of the CdS in seawater conditions up to 30 hours. The apparent quantum yield of the CQD@CdS photocatalyst developed was reported to be up to 20.07%. It is hoped that this research can provide a reliable approach to devising cost-effective and high-performance hybrid photocatalysts, that can effectively support for industrial applications.

Author contributions

Bishal Kumar Nahak drafted the manuscript, designed and performed the experiments, and analyzed the data, Fan-Gang Tseng designed the experiments, supervised the research, and reviewed and modified the manuscript.

Conflicts of interest

There are no conflicts to declare.

Acknowledgements

The authors would like to acknowledge Satish Bolloju from Department of Chemical Engineering, National Taiwan University for use of the X-ray diffraction facility; the Department of Chemical Engineering and Engineering and System Science, National Tsing Hua University for allowing use their of their scanning electron microscope and transmission electron microscope; the Department of Materials Science Engineering, National Yang Ming Chiao Tung University for help with the X-ray photoelectron auger spectroscopy; the Instrumentation Center at National Tsing Hua University for their support with the electron paramagnetic resonance and induction-coupled plasma mass spectroscopy. The authors are thankful for the financial support for this work from the Ministry of Science and Technology, Taiwan (MOST 110-2634-F-007-023-MY3), and the Ministry of Education, Taiwan, Frontier Research Centre on Fundamental and Applied Sciences of Matters (MOE-111QR001I5).

References

1 B. K. Nahak, S. Preetam, D. Sharma, S. K. Shukla, M. Syväjärvi, D.-C. Toncu and A. Tiwari, *Renewable Sustainable Energy Rev.*, 2022, **161**, 112393.
2 A. Kudo and Y. Miseki, *Chem. Soc. Rev.*, 2009, **38**, 253–278.
3 Y. Ma, X. Wang, Y. Jia, X. Chen, H. Han and C. Li, Titanium Dioxide-Based Nanomaterials for Photocatalytic Fuel Generations, *Chem. Rev.*, 2014, **114**, 9987–10043.
4 X. Wang, K. Maeda, A. Thomas, K. Takanabe, G. Xin, J. M. Carlsson, K. Domen and M. Antonietti, *Nat. Mater.*, 2009, **8**, 76–80.
5 N. Z. Muradov and T. N. Veziroğlu, *Int. J. Hydrogen Energy*, 2008, **33**, 6804–6839.
6 M. G. Walter, E. L. Warren, J. R. McKone, S. W. Boettcher, Q. Mi, E. A. Santori and N. S. Lewis, Solar Water Splitting Cells, *Chem. Rev.*, 2010, **110**, 6446–6473.
7 C. Acar, I. Dincer and C. Zamfirescu, *Int. J. Energy Res.*, 2014, **38**, 1903–1920.
8 H. Ahmad, S. K. Kamarudin, L. J. Minggu and M. Kassim, *Renewable Sustainable Energy Rev.*, 2015, **43**, 599–610.
9 J. Gong, S. B. Darling and F. You, *Energy Environ. Sci.*, 2015, **8**, 1953–1968.
10 A. Fujishima and K. Honda, *Nature*, 1972, **238**, 37–38.
11 T. Hisatomi, J. Kubota and K. Domen, *Chem. Soc. Rev.*, 2014, **43**, 7520–7535.
12 C. Gomes Silva, R. Juárez, T. Marino, R. Molinari and H. García, *J. Am. Chem. Soc.*, 2011, **133**, 595–602.
13 X. Chen, S. Shen, L. Guo and S. S. Mao, *Chem. Rev.*, 2010, **110**, 6503–6570.
14 S. Cao, J. Low, J. Yu and M. Jaroniec, *Adv. Mater.*, 2015, **27**, 2150–2176.
15 G. Di, Z. Zhu, Q. Dai, H. Zhang, X. Shen, Y. Qiu, Y. Huang, J. Yu, D. Yin and S. Küppers, *Chem. Eng. J.*, 2020, **379**, 122296.
16 R. S. Sprick, J.-X. Jiang, B. Bonillo, S. Ren, T. Ratvijitvech, P. Guiglion, M. A. Zwijnenburg, D. J. Adams and A. I. Cooper, *J. Am. Chem. Soc.*, 2015, **137**, 3265–3270.
17 T. Arshad, S. A. Khan, M. Faisal, Z. Shah, K. Akhtar, A. M. Asiri, A. A. Ismail, B. G. Alhogbi and S. B. Khan, *J. Mol. Liq.*, 2017, **241**, 20–26.
18 Y. Qiao, T. Cheisson, B. C. Manor, P. J. Carroll and E. J. Schelter, *Chem. Commun.*, 2019, **55**, 4067–4070.
19 H. M. Lwin, W. Zhan, S. Song, F. Jia and J. Zhou, *Chem. Phys. Lett.*, 2019, **736**, 136806.
20 A. M. Al-Hamdi, U. Rinner and M. Sillanpää, *Process Saf. Environ. Prot.*, 2017, **107**, 190–205.
21 P. K. Labhane and G. H. Sonawane, *Inorg. Chem. Commun.*, 2020, **113**, 107809.
22 Y. Jia, Y. Ma, L. Zhu, J. Dong and Y. Lin, *Chem. Phys.*, 2019, **521**, 1–4.
23 R. Roshan, B. K. Nahak, D. Mahata, P. Yadav, S. Panda, S. Patra, S. S. Mahato, A. Tiwari and S. Mahata, *Energy Convers. Manage.*, 2023, **283**, 116917.
24 N. K. Elumalai, C. Vijila, R. Jose, A. Uddin and S. Ramakrishna, *Mater. Renew. Sustainable Energy*, 2015, **4**, 11.
25 Y. Xu, Y. Huang and B. Zhang, *Inorg. Chem. Front.*, 2016, **3**, 591–615.
26 M. Tayyab, Y. Liu, Z. Liu, Z. Xu, W. Yue, L. Zhou, J. Lei and J. Zhang, *Chem. Eng. J.*, 2023, **455**, 140601.
27 S. A. Ali and T. Ahmad, *Int. J. Hydrogen Energy*, 2022, **47**, 29255–29283.
28 P. Garg, P. Bhauriyal, A. Mahata, K. S. Rawat and B. Pathak, *Chem. Phys. Chem.*, 2019, 383–391.
29 C. M. Wolff, P. D. Frischmann, M. Schulze, B. J. Bohn, R. Wein, P. Livadas, M. T. Carlson, F. Jäckel, J. Feldmann, F. Würthner and J. K. Stolarczyk, *Nat. Energy*, 2018, **3**, 862–869.
30 B. Nahak, R. Roshan, N. Jhariya, S. Bolloju, B. Pandit, S. Mahato and S. Mahata, *Surf. Interfaces*, 2023, **42**, 103351.
31 S. Panda, A. Sahu, A. Patra, S. Panda, B. K. Nahak, B. N. Patra, S. S. Mahato and S. Mahata, *Mater. Today: Proc.*, 2021, **47**, 1197–1202.
32 Y. Xia, K. D. Gilroy, H.-C. Peng and X. Xia, *Angew. Chem., Int. Ed.*, 2017, **56**, 60–95.
33 A. R. Tao, S. Habas and P. Yang, *Small*, 2008, **4**, 310–325.
34 H. Wang, P. Fang, Z. Chen and S. Wang, *Appl. Surf. Sci.*, 2007, **253**, 8495–8499.
35 M. Pattabi, B. Saraswathi Amma and K. Manzoor, *Mater. Res. Bull.*, 2007, **42**, 828–835.
36 T. Thongtem, A. Phuruangrat and S. Thongtem, *Ceram. Int.*, 2009, **35**, 2817–2822.
37 D. Hao, C. Liu, X. Xu, M. Kianinia, I. Aharonovich, X. Bai, X. Liu, Z. Chen, W. Wei, G. Jia and B.-J. Ni, *New J. Chem.*, 2020, **44**, 20651–20658.
38 Q. Wang, S. Zhu, S. Zhao, C. Li, R. Wang, D. Cao and G. Liu, *Fuel*, 2022, **322**, 124163.
39 B. K. Nahak, D. Mahata, N. Jhariya, P. Yadav, S. Panda, S. S. Sahu, K. Swatishree, A. P. Khedulkar, S. Bolloju, B. Pandit,

S. S. Mahato and S. Mahata, *Ceram. Int.*, 2023, **49**, 32104–32115.
40 Q. Lin, S. Liang, J. Wang, R. Zhang, G. Liu and X. Wang, *ACS Sustainable Chem. Eng.*, 2023, **11**, 3093–3102.
41 X. Li, J. Wang, J. Zhang, C. Zhao, Y. Wu and Y. He, *J. Colloid Interface Sci.*, 2022, **607**, 412–422.
42 C. Liu, Y. Xiao, W. Wan, Y. Wei, Y. Cao, L. Hong, Y. Wang, J. Chen, Q. Zhang and H. Jing, *Appl. Catal., B*, 2023, **325**, 122394.
43 L. Zhang, X. Jiang, Z. Jin and N. Tsubaki, *J. Mater. Chem. A*, 2022, **10**, 10715–10728.
44 H. Sun, Z. Xiao, Z. Zhao, S. Zhai and Q. An, *Appl. Surf. Sci.*, 2023, **611**, 155631.
45 Y. Su, X. Xu, R. Li, X. Luo, H. Yao, S. Fang, K. Peter Homewood, Z. Huang, Y. Gao and X. Chen, *Chem. Eng. J.*, 2022, **429**, 132241.
46 X. Bai, X. Wang, X. Lu, Y. Liang, J. Li, L. Wu, H. Li, Q. Hao, B.-J. Ni and C. Wang, *J. Hazard. Mater.*, 2020, **398**, 122897.
47 Z. Jin, T. Wei, F. Li, Q. Zhang and L. Xu, *New J. Chem.*, 2020, **44**, 3471–3477.
48 H. Yu, W. Zhong, X. Huang, P. Wang and J. Yu, *ACS Sustainable Chem. Eng.*, 2018, **6**, 5513–5523.
49 K. Li, M. Han, R. Chen, S.-L. Li, S.-L. Xie, C. Mao, X. Bu, X.-L. Cao, L.-Z. Dong, P. Feng and Y.-Q. Lan, *Adv. Mater.*, 2016, **28**, 8906–8911.
50 Z. Ai, G. Zhao, Y. Zhong, Y. Shao, B. Huang, Y. Wu and X. Hao, *Appl. Catal., B*, 2018, **221**, 179–186.
51 I. Velo-Gala, J. J. López-Peñalver, M. Sánchez-Polo and J. Rivera-Utrilla, *Appl. Catal., B*, 2017, **207**, 412–423.
52 K. S. Bhavsar, P. K. Labhane, R. B. Dhake and G. H. Sonawane, *Inorg. Chem. Commun.*, 2019, **104**, 134–144.
53 J. Ge, Y. Zhang and S.-J. Park, *Materials*, 2019, **12**, 1916.
54 H. Li, Z. Kang, Y. Liu and S.-T. Lee, *J. Mater. Chem.*, 2012, **22**, 24230–24253.
55 H. Ming, Z. Ma, Y. Liu, K. Pan, H. Yu, F. Wang and Z. Kang, *Dalton Trans.*, 2012, **41**, 9526–9531.
56 C. Zhu, Y. Fu, C. Liu, Y. Liu, L. Hu, J. Liu, I. Bello, H. Li, N. Liu, S. Guo, H. Huang, Y. Lifshitz, S.-T. Lee and Z. Kang, *Adv. Mater.*, 2017, **29**, 1701399.
57 Y. Wang, X. Liu, J. Liu, B. Han, X. Hu, F. Yang, Z. Xu, Y. Li, S. Jia, Z. Li and Y. Zhao, *Angew. Chem.*, 2018, **130**, 5867–5873.
58 C. Zhu, C. Liu, Y. Zhou, Y. Fu, S. Guo, H. Li, S. Zhao, H. Huang, Y. Liu and Z. Kang, *Appl. Catal., B*, 2017, **216**, 114–121.
59 S. Sharma, V. Dutta, P. Singh, P. Raizada, A. Rahmani-Sani, A. Hosseini-Bandegharaei and V. K. Thakur, *J. Cleaner Prod.*, 2019, **228**, 755–769.
60 Y. Lei, C. Yang, J. Hou, F. Wang, S. Min, X. Ma, Z. Jin, J. Xu, G. Lu and K.-W. Huang, *Appl. Catal., B*, 2017, **216**, 59–69.
61 J. Guo, M. Guo, D. Jia, X. Song and F. Tong, *Chem. Phys. Lett.*, 2016, **659**, 66–69.
62 S. P. Smrithi, N. Kottam, A. Narula, G. M. Madhu, R. Mohammed and R. Agilan, *J. Colloid Interface Sci.*, 2022, **627**, 956–968.
63 C. Tang, Y. Zhang, J. Han, Z. Tian, L. Chen and J. Chen, *Environ. Pollut.*, 2020, **262**, 114246.
64 C. Zhu, C. Liu, Y. Fu, J. Gao, H. Huang, Y. Liu and Z. Kang, *Appl. Catal., B*, 2019, **242**, 178–185.
65 D. Gogoi, R. Koyani, A. K. Golder and N. R. Peela, *Sol. Energy*, 2020, **208**, 966–977.
66 Y.-J. Yuan, D. Chen, Z.-T. Yu and Z.-G. Zou, *J. Mater. Chem. A*, 2018, **6**, 11606–11630.
67 H. Arandiyan, S. S. Mofarah, C. C. Sorrell, E. Doustkhah, B. Sajjadi, D. Hao, Y. Wang, H. Sun, B.-J. Ni, M. Rezaei, Z. Shao and T. Maschmeyer, *Chem. Soc. Rev.*, 2021, **50**, 10116–10211.
68 M. Kong, Y. Li, X. Chen, T. Tian, P. Fang, F. Zheng and X. Zhao, *J. Am. Chem. Soc.*, 2011, **133**, 16414–16417.
69 H. Zhang, H. Wang, Y. Wang and B. Xin, *Appl. Surf. Sci.*, 2020, **512**, 145751.
70 C. Carrillo-Carrión, S. Cárdenas, B. M. Simonet and M. Valcárcel, *Chem. Commun.*, 2009, 5214–5226.
71 H. Li, W. Kong, J. Liu, N. Liu, H. Huang, Y. Liu and Z. Kang, *Carbon*, 2015, **91**, 66–75.
72 A. Sharma, T. Gadly, S. Neogy, S. K. Ghosh and M. Kumbhakar, *J. Phys. Chem. Lett.*, 2017, **8**, 1044–1052.
73 M. Ma, Y. Liu, Y. Wei, D. Hao, W. Wei and B.-J. Ni, *J. Environ. Manage.*, 2021, **294**, 113046.
74 M. Wang, Z. Wang, B. Zhang, W. Jiang, X. Bao, H. Cheng, Z. Zheng, P. Wang, Y. Liu, M.-H. Whangbo, Y. Li, Y. Dai and B. Huang, *ACS Catal.*, 2020, **10**, 13031–13039.
75 A.-M. Alam, B.-Y. Park, Z. Khan Ghouri, M. Park and H.-Y. Kim, *Green Chem.*, 2015, **17**, 3791–3797.
76 B. K. Nahak, R. Roshan, S. D. Roy, A. Patra, A. Sahu, S. Panda, S. Panda, S. S. Mahato and S. Mahata, *J. Mater. Sci.: Mater. Electron.*, 2022, **33**, 15191–15208.
77 A. Sachdev and P. Gopinath, *Analyst*, 2015, **140**, 4260–4269.
78 Y. Pei, R. Pei, X. Liang, Y. Wang, L. Liu, H. Chen and J. Liang, *Sci. Rep.*, 2016, **6**, 21551.
79 K. S. Bhavsar, P. K. Labhane, R. B. Dhake and G. H. Sonawane, *Chem. Phys. Lett.*, 2020, **744**, 137202.
80 L. Wu, J. C. Yu and X. Fu, *J. Mol. Catal. A: Chem.*, 2006, **244**, 25–32.
81 X. Bai, X. Wang, T. Jia, L. Guo, D. Hao, Z. Zhang, L. Wu, X. Zhang, H. Yang, Y. Gong, J. Li and H. Li, *Appl. Catal., B*, 2022, **310**, 121302.
82 A. Veamatahau, B. Jiang, T. Seifert, S. Makuta, K. Latham, M. Kanehara, T. Teranishi and Y. Tachibana, *Phys. Chem. Chem. Phys.*, 2015, **17**, 2850–2858.
83 W. Zou, B. Gao, Y. S. Ok and L. Dong, *Chemosphere*, 2019, **218**, 845–859.
84 Q. Fan, Y. Huang, C. Zhang, J. Liu, L. Piao, Y. Yu, S. Zuo and B. Li, *Catal. Today*, 2016, **264**, 250–256.
85 M. Moniruzzaman and J. Kim, *Appl. Surf. Sci.*, 2021, **552**, 149372.
86 H. Ait Ahsaine, M. Ezahri, A. Benlhachemi, B. Bakiz, S. Villain, F. Guinneton and J.-R. Gavarri, *Ceram. Int.*, 2016, **42**, 8552–8558.
87 M. Sachs, R. S. Sprick, D. Pearce, S. A. J. Hillman, A. Monti, A. A. Y. Guilbert, N. J. Brownbill, S. Dimitrov, X. Shi,

F. Blanc, M. A. Zwijnenburg, J. Nelson, J. R. Durrant and A. I. Cooper, *Nat. Commun.*, 2018, **9**, 4968.
88 W. Shi, F. Guo, M. Li, Y. Shi and Y. Tang, *Sep. Purif. Technol.*, 2019, **212**, 142–149.
89 N. N. Yunus, F. Hamzah, M. S. So'aib and J. Krishnan, *IOP Conf. Ser.: Mater. Sci. Eng.*, 2017, **206**, 012092.
90 Y. Tang, X. Hu and C. Liu, *Phys. Chem. Chem. Phys.*, 2014, **16**, 25321–25329.
91 S. Feizpoor, S. Rahim Pouran and A. Habibi-Yangjeh, *Mater. Sci. Semicond. Process.*, 2023, **162**, 107444.
92 J. Shi, J. Zhang, Z. Cui, S. Chu, Y. Wang and Z. Zou, *Dalton Trans.*, 2022, **51**, 5841–5858.
93 M. Sabri, A. Habibi-Yangjeh, S. Rahim Pouran and C. Wang, *Catal. Rev.*, 2023, **65**, 118–173.
94 A. Habibi-Yangjeh and K. Pournemati, *Crit. Rev. Environ. Sci. Technol.*, 2023, 1–31.